Available online at www.sciencedirect.com
SCIENCE DIRECT®
Journal of Power Sources 124 (2003) 564–571
JOURNAL OF POWER SOURCES
www.elsevier.com/locate/jpowsour

Electrochemical study of $LaNi_{3.55}Mn_{0.4}Al_{0.3}Co_{0.75}$ by cavity microelectrode in 7 mol l^{-1} KOH solution

V. Vivier [a], C. Cachet-Vivier [a,*], J.-Y. Nédélec [a], L.T. Yu [a], J.-M. Joubert [b], A. Percheron-Guégan [b]

[a] *Laboratoire d'Electrochimie Catalyse et Synthèse Organique, UMR 7582 CNRS-Université Paris 12, Institut des Sciences Chimiques Seine-Amont, 2-8 rue H. Dunant, 94320 Thiais, France*
[b] *Laboratoire de Chimie Métallurgique des Terres Rares, UPR 209 CNRS, Institut des Sciences Chimiques Seine-Amont, 2-8 rue H. Dunant, 94320 Thiais, France*

Received 3 March 2003; received in revised form 26 June 2003; accepted 30 June 2003

Abstract

The electrochemical behavior of $LaNi_{3.55}Mn_{0.4}Al_{0.3}Co_{0.75}$ material was investigated with the help of a cavity microelectrode. The cyclic voltammetry study versus the scan rate evidenced the formation of a passivation layer, which is characterized by a positive current during the cathodic sweep. The performances of the $LaNi_{3.55}Mn_{0.4}Al_{0.3}Co_{0.75}$ compound as a negative electrode for nickel–metal hydride (Ni–MH) battery can also be determined with the cavity microelectrode. It was shown that even in drastic potential sweep conditions, the material exhibits a very good reversibility during several thousands of cycles.
© 2003 Elsevier B.V. All rights reserved.

Keywords: Hydrides; AB_5 compound; Cavity microelectrode; Battery

1. Introduction

$LaNi_5$ and its metal substituted derivatives reversibly absorb hydrogen around room temperature and pressure by solid–gas as well as by electrochemical reactions. Among the possible applications of those hydrides, their use as negative electrode materials for nickel–metal hydride (Ni–MH) alkaline batteries has been the subject of a lot of studies [1–8]. Those batteries replace nickel–cadmium systems because of the increased capacity and the reduced toxicity. Research on the alloy composition to improve both thermodynamic and cycling properties of the electrode material has led to the set-up of multi-substituted compositions like $RENi_{3.55}Mn_{0.4}Al_{0.3}Co_{0.75}$ (RE, rare earth elements) [9,10].

Electrochemical characterizations of those compounds are usually performed with the usual composite electrode [5,7], which consists in powder material mixed with graphite and Teflon binder pressed on an extended current collector. However, the cyclic voltammetry behavior for high scan rate (v) cannot be investigated with such an electrode, since the highest rate at which the signal can be analyzed is lower than $1\,mV\,s^{-1}$. This restriction is ascribed to large ohmic drop and capacitive current. In previous papers [11–13], we have shown that the use of cavity microelectrode (CME) allows the study at scan rates up to a few tens $V\,s^{-1}$ (this limit depending on both the studied material and the electrode size), and the determination of the oxydoreduction mechanism [12]. Moreover, we have pointed out that CME was a useful technique for achieving long cycling tests in a short lapse of time [13,14].

This paper is devoted to the electrochemical behavior of $LaNi_{3.55}Mn_{0.4}Al_{0.3}Co_{0.75}$ powder when submitted to potentiodynamic conditions at scan rates up to $1\,V\,s^{-1}$ and cycling up to a few thousands of cycles by means of the CME.

2. Experimental

2.1. Preparative procedure

The intermetallic compound was synthesized by induction melting of the pure elements, followed by adequate annealing. Homogeneity and single-phase characteristics were checked by X-ray diffraction and electron microprobe analysis [15]. The material is ground by means of a pestle. The grains have an irregular shape and their size is between a few μm and 20–30 μm (Fig. 1). After grinding,

* Corresponding author. Tel.: +33-149-7811-37; fax: +33-149-7811-48.
E-mail address: cachet@glvt-cnrs.fr (C. Cachet-Vivier).

0378-7753/$ – see front matter © 2003 Elsevier B.V. All rights reserved.
doi:10.1016/S0378-7753(03)00796-1

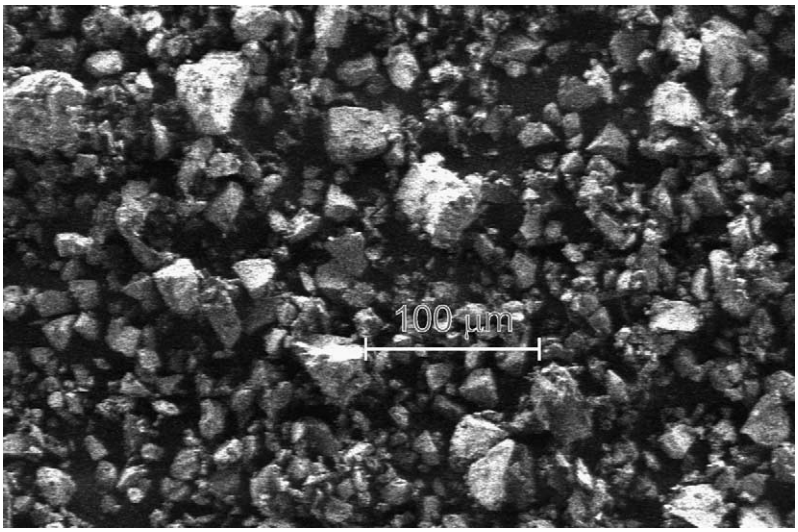

Fig. 1. SEM photography of $LaNi_{3.55}Mn_{0.4}Al_{0.3}Co_{0.75}$.

the material is immediately submitted to an electrochemical study.

2.2. Electrochemical devices

Electrochemical measurements were carried out with a classical three-electrode cell. The working electrode was a home-made cavity microelectrode previously described [11–13]. The reference and counter electrode were an Hg/HgO (7 mol l^{-1} KOH) electrode and a stainless steel wire, respectively. Both were in a separated compartment. The electrolyte was a 7 mol l^{-1} KOH solution that was deoxygenated by bubbling with Ar gas. Electrochemical measurements were performed using an Autolab PGSTAT 30 potentiostat. The cleanliness of the cavity volume was checked before each experiment by recording background voltammograms of the Pt-current collector.

For all experiments, no graphite was mixed with the material since it is a sufficiently good electronic conductor. The cavity of the microelectrode was filled up with material grains using the electrode as a pestle. We ensured that the cavity was conveniently filled up by observing it with a microscope (Olympus BX30) equipped with a numerical camera unit (DP10). After every set of electrochemical experiments, we ensured that the material was still present within the microcavity. The cavity was unloaded by washing it with an ultrasonic cleaner in 5 mol l^{-1} HCl solution for 5 min.

3. Results

3.1. Voltammogram descriptions

Stable voltammograms are observed during cycling in the scan range spreading from −1.15 to 0.25 V/Hg/HgO. Fig. 2 illustrates the general shape of voltammograms we recorded with the CME at 0.05 V s^{-1}. It shows that the electrochemical response of the material (solid-line curve) is distinguishable from the platinum current collector one (dotted-line curve). Fig. 3a and c represent voltammograms recorded at various scan rates.

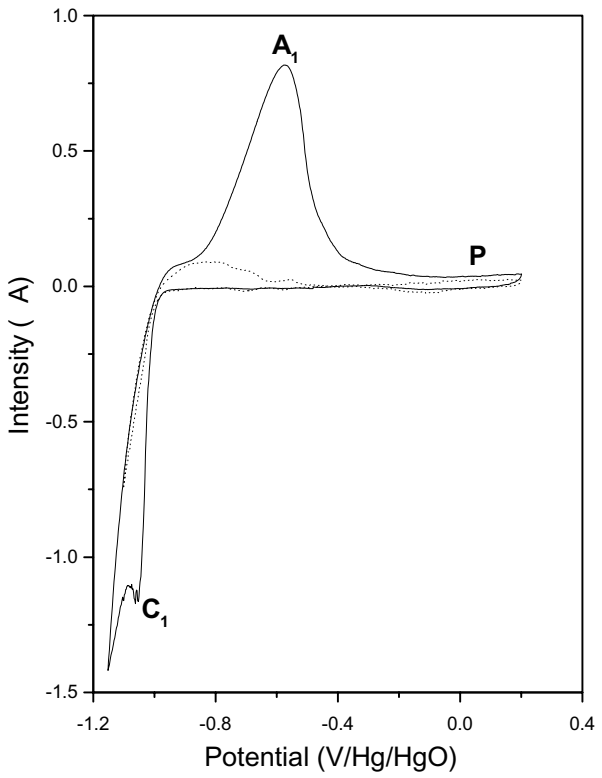

Fig. 2. Voltammograms recorded on $LaNi_{3.55}Mn_{0.4}Al_{0.3}Co_{0.75}$ powder with a 25 µm diameter CME at 50 mV s^{-1} in a 7 mol l^{-1} KOH solution (solid-line), and with an empty CME in the same conditions (dotted-line).

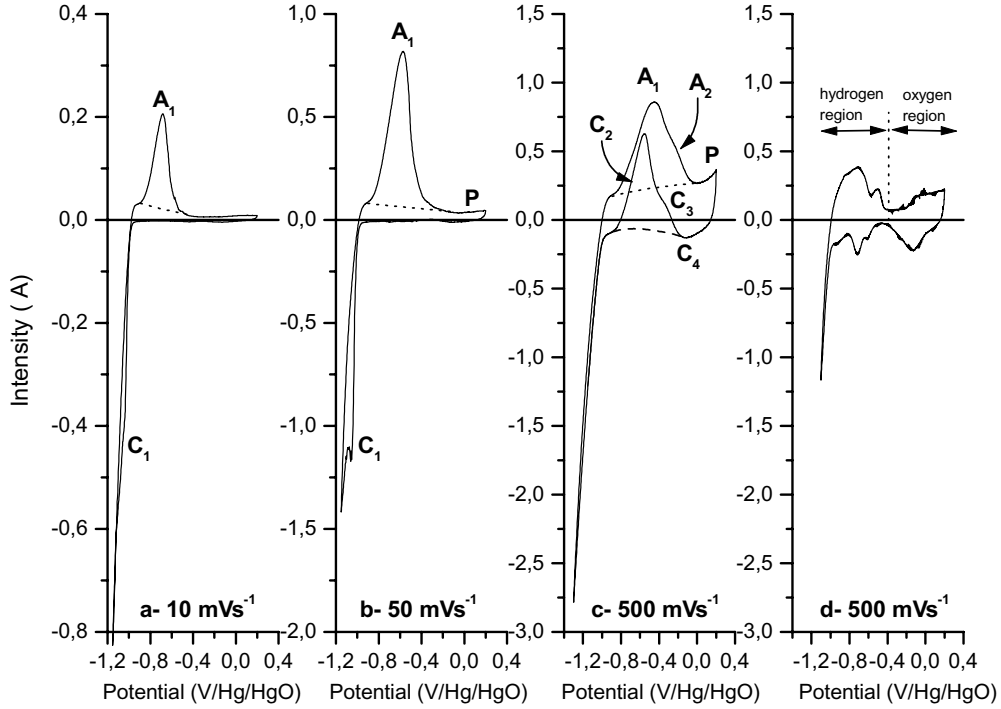

Fig. 3. (a–c) Voltammograms recorded on $LaNi_{3.55}Mn_{0.4}Al_{0.3}Co_{0.75}$ powder with a 25 μm diameter CME at various scan rates. (d) Voltammogram recorded on the empty cavity at 500 mV s^{-1}.

At low scan rates ($v < 0.05$ V s^{-1}), we observe the following peaks:

- An ill-defined cathodic peak C_1 that merges with the solvent reduction wall and progressively disappears while increasing scan rate. It is attributed to hydrogen insertion in the compound.
- An anodic peak A_1, the potential of which vary between −0.7 and −0.5 V/Hg/HgO. It is attributed to hydrogen desorption. Moreover, the total cathodic exchanged charge is equal to the anodic one, which is consistent with battery material application.
- A plateau P that follows the anodic peaks at the end of the anodic scan. Its intensity (i_P) is proportional to the scan rate, which indicates that it is not a diffusion plateau like often observed for insertion materials. It should rather be identified as due to a capacitive current.

As the scan rate increases to reach few hundred of mV s^{-1}, voltammogram shapes significantly change (Fig. 3c).

- The A_1 peak enlarges significantly to show a shoulder A_2.
- A positive-current peak C_2 located within the potential range of the peak A_1 appears during the reduction step. It is preceded by a small shoulder C_3, which is similar to A_2, observed during the anodic sweep.
- The small cathodic peak C_4 (located at ca. −0.15 V/Hg/HgO) is similar to the cathodic peak recorded on the empty CME at the same scan rate (Fig. 3d). The curve corresponding to the collector metal–surface exhibits the two well-known regions: the hydrogen-region where occurs hydrogen electroadsorption and the oxygen-region where occur the oxides formation and their reduction [16].

3.2. Voltammogram characteristics

From Figs. 2 and 3, we can define various voltammogram characteristics for a quantitative description. We point out the potential E_Y and the intensity i_Y of each peak Y (Y = a_1, c_1, c_2), the area S_Y of the peaks A_1 and C_2. The anodic characteristics are evaluated from the baseline drawn (in dotted-line), by interpolating the capacitive current. The peak C_2 area is calculated considering the baseline drawn in dashed-line. We did not determine the area of the peak C_1 because it is not possible to clearly distinguish its contribution from that of the water reduction. The measurement of the peak area allows evaluating the exchanged charge associated to the current exchange through the relationships:

$$Q_Y = \frac{S_Y}{v} \quad (1)$$

Fig. 4a shows the variation of the peak potentials E_{C_1}, E_{C_2}, and E_{A_1} versus v, in a logarithmic scale. For $v < 0.05$ V s^{-1}, E_{C_1} linearly decreases with a slope $dE_{C_1}/d\log v$ of −20 mV, whereas for $v > 0.05$ V s^{-1}, the slope is −150 mV. Furthermore, we note that this transition range corresponds to the appearance of the positive current (peak C_2). Contrarily, E_{A_1} increases with a slope of +190 mV up to 0.3 V s^{-1}, and is quite constant for $v > 0.3$ V s^{-1}. Fig. 4b shows the

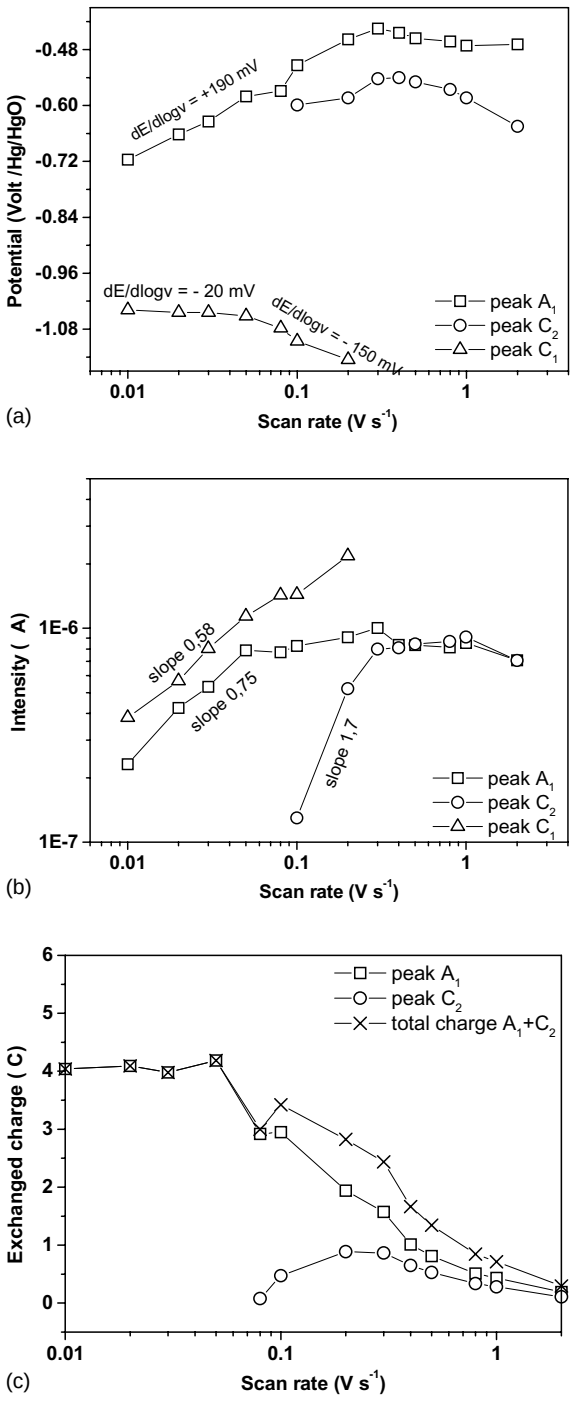

Fig. 4. Voltammogram characteristics-scan rate profiles: (a) peak potential-scan rate; (b) peak intensity-scan rate; (c) exchanged charges-scan rate.

variations of i_{C_1} and i_{A_2}, versus v, in bilogarithmic scale. We note that $\log(i_{C_1})$ is proportional to $\log(v)^m$ with $m = 0.58$. $\text{Log}(i_{A_1})$ varies as $\log(v)^m$ where $m = 0.75$ when $v < 0.05\,\text{V s}^{-1}$ and $m = 0$ for $v > 0.05\,\text{V s}^{-1}$. The slopes are different from 1 that indicates a diffusion mechanism.

Fig. 4c concerns the variation of the positive exchanged charge during the anodic scan (peak A_1, curve □), the cathodic scan (peak C_2, curve ○) and the total positive charge

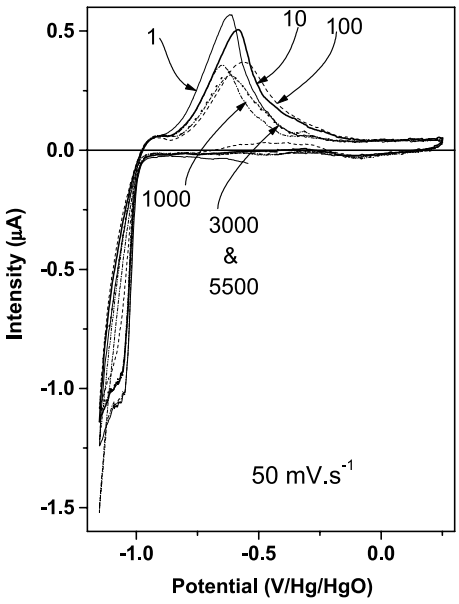

Fig. 5. Evolution of the voltammograms for different cycle numbers. Each curve is labeled by its cycle number.

(peaks $A_1 + C_2$). The exchanged charge Q_{A_1} is constant when v is lower than $0.05\,\text{V s}^{-1}$. This indicates that the number of accessible sites in the material that are implicated in the electrochemical reactions is constant. Moreover in that scan rate domain, the positive charge between -1 and $0.2\,\text{V/Hg/HgO}$ is nearly equal to the total negative charge between -1 and $-1.2\,\text{V/Hg/HgO}$. It signifies that the H_2 produced on the solvent reduction wall contributes to chemically charge the material. Q_{A_1} strongly decreases for the highest values of the scan rate which corresponds to the merging of the peak C_1 with the reduction wall of the solvent. The production of H_2 is thus predominant in front of the H insertion in the material. Moreover, the graph shows that the contribution of the peak C_2 can be considered as negligible when compared with the total exchanged charge.

3.3. Long cycling evolution

Fig. 5 shows the evolution of the voltammogram for different numbers of cycle for a battery test experiment performed at $V = 50\,\text{mV s}^{-1}$. Fig. 6 shows the variations of the peak potential E_{A_1} (graph a), and of the peak intensity i_{A_1} (graph b). As it is difficult to determine the amount of material included in the cavity, graph c is related to the normalized charge. It is defined by the ratio of anodic exchanged charge $Q_A/Q_A^{\max}$, where $Q_A^{\max}$ is the maximum anodic exchanged charge during a sweep of the cycling. For all the graphs, two regions can be defined; the boundary of which is around the 800th cycle. Within the region I, there is an erratic variation of the voltammogram characteristics. The anodic peak potential varies within a 90 mV amplitude range, whereas i_{A_1} and Q_A variations represent 50 and 20% of their maximum value, respectively. In the region II, we

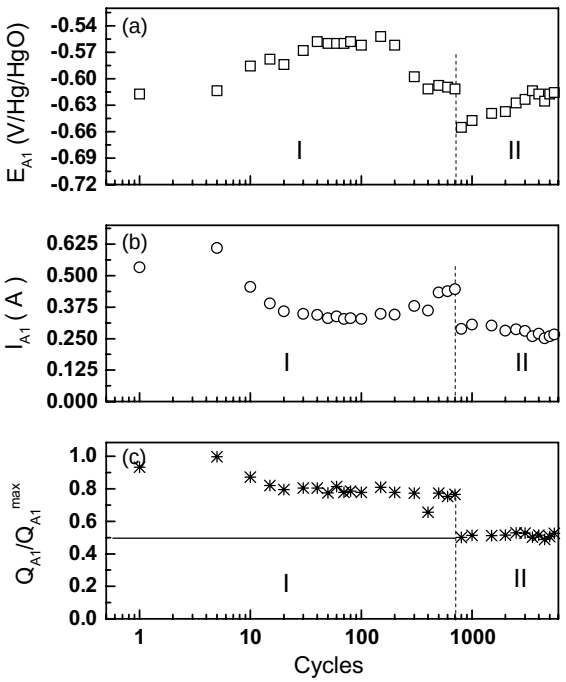

Fig. 6. Evolution of the peak potential (a), the peak intensity (b), and the ratio of anodic exchanged charge Q_A/maximum exchanged charge (Q_A^{max}) (c) versus the cycle number.

observe a more regular variation of the previous parameters: E_{A_1} shifts toward the positive potential by around 30 mV, whereas i_{A_1} and Q_{A_1} remain constant after a decrease of 7 and 25%, respectively. That still can be considered as a quite stable behavior. The boundary between the two regions corresponds to a sudden loss of electrical contact between grains. The transition from an erratic behavior before the 800th cycle and quite stable behavior can be ascribed to a decrease of grains compacting within the cavity.

4. Discussion

4.1. Effect of the geometrical features of a CME on the exchanged charges

The filling of the microcavity depends on both shape and size of the grains. The theoretical maximum amount of included material is obtained assuming a cubic stacking of small spheres (that represent material grains). The resulting ratio between the interstice volume and the grain sphere volume is independent of the sphere radius, and is ca. 0.9. The volume of interstices is thus similar to that of the material one. As a result, for a 25 μm diameter CME, the depth of which is 15 μm, the occupied volume of cavity is ca. 3.7×10^{-9} cm^3. The maximum exchangeable charge is given by the Faraday's law:

$$Q^{\max} = \frac{nF \times \rho \times 3.7 \times 10^{-9}}{M} \quad (2)$$

where F is the Faraday, M is the molecular weight of the material ($M = 421.5\,\mathrm{g\,mol^{-1}}$), ρ its density ($\rho = 7.8$) and n is the number of exchanged electrons, according to the following reduction reaction (x is the insertion rate):

$$\langle AB_5 \rangle + x\mathrm{e} + x\mathrm{H_2O} \rightleftarrows \langle AB_5H_x \rangle + x\mathrm{OH^-} \quad \text{with } 0 \le x \le n \quad (3)$$

For $LaNi_5$, n is comprised between 6 and 6.5, whereas for the tri-substituted material, the maximum n value is 5.5. This corresponds to a theoretical exchangeable charge of 36 mC for $LaNi_{3.55}Mn_{0.4}Al_{0.3}Co_{0.75}$. From our experiments, the exchanged charge is actually around 4 mC. A priori, several causes can be invoked for explaining the charge lack:

- First, the irregular shape of the grains does not favor the stacking within the microcavity. Moreover, the material grain is subjected to volume expansion and contraction during hydrogen absorption and desorption, respectively. This could make more difficult the electrical contacts between the grains and between grains and metal current collector.
- Second, the amount of available water within the interstices could be insufficient since the insertion of H needs the consumption of H_2O molecules. The total amount of H_2O inside the interstices is about 2×10^{-10} moles. From the Eq. (3), the consumption of 1 mole of the material during the electrochemical process is accompanied by the consumption of 5.5 moles of water. Thus, a quantitative reduction reaction of the material (6.15×10^{-11} mole) needs 3.38×10^{-10} mole of water. The amount of water inside the cavity is not sufficient for reducing all the electroactive sites of the material included in the microcavity.
- Third, the reduction reaction is partial and may concern only the peripheral sites and those located within the layers near the surface. Such a behavior could be attributed to a limited diffusion of the H inserted. The latter case must be ruled out because the exchanged charge does not vary significantly against the scan rate. The two first assumptions may be a possible explanation of the difference between theoretical and experimental value of the exchanged charge.

4.2. Comments on peak C_1

This peak corresponds to the insertion of H within the material. The overall mechanism generally ascribed is a charge transfer reaction (Heyrovsky step) followed by a phase transfer reaction between adsorbed and absorbed hydrogen and by the mass transfer of hydrogen into the material bulk [17–19]. Taking account of the available data, we propose the following mechanism:

- Electron transfer reaction and H adsorption:

$$\langle AB_5 \rangle_0 + \mathrm{e} + \mathrm{H_2O} \rightleftarrows \langle AB_5H \rangle_0^{\mathrm{ads}} + \mathrm{OH^-} \quad (4)$$

$\langle AB_5\rangle_0$ and $\langle AB_5H\rangle_0^{ads}$ are an oxidized (H-free) site that can be reduced and a reduced site with adsorbed hydrogen, respectively. The subscript 0 indicates that this reaction occurs at the interface of the material.

- Phase transfer reaction:

$$\langle AB_5H\rangle_0^{ads} \underset{k_{-1}}{\overset{k_1}{\rightleftarrows}} \langle AB_5H\rangle_0^{abs} \quad (5)$$

the superscripts ads and abs indicate that the hydrogen is adsorbed and absorbed, respectively. k_1 and k_{-1} are the chemical kinetic constants of this reaction.

- Diffusion reaction:

$$\langle AB_5H\rangle_0^{abs} \underset{k_{-2}}{\overset{k_2}{\rightleftarrows}} \langle AB_5H\rangle_{bulk}^{abs} \quad (6)$$

$\langle AB_5H\rangle_{bulk}^{abs}$ refers to the hydrogen absorbed in the material bulk, k_2 and k_{-2} are the kinetic constants of this reaction. However, with such a global reaction pathway for describing the diffusion in the material bulk, the kinetic constants k_2 and k_{-2} depend on both material geometry and grain size [20]. On the other hand, it was shown that the multilayer model evolved by Laviron and co-workers [21–23], Andrieux and Saveant [24] can easily be transposed for describing the insertion of species into a material bulk, whatever its geometry [20]. As a result, assuming that the material grain consists in a stacking of elementary layers as represented in Fig. 7a, the overall diffusion reaction is to be seen as successive elementary reactions characterizing the displacement of H between sites located in two adjacent layers (Fig. 7b). By construction of the model, all the layers are identical and represent a monolayer of $\langle AB_5\rangle$ sites. Thus, the total amount of H that can be inserted is identical for each layer and the chemical kinetic constants of each reaction are then equal for each layer. It shows that with this representation, values of kinetic constants are independent of the geometry of the material. Nevertheless, this description needs the knowledge of the grain geometry and the grain size to describe each layer. For a material constituted of n layers, the diffusion reaction is thus summarized by the following set of reactions $(7)_i$ $(1 \le i \le n)$:

$$\langle AB_5H\rangle_0 + \langle AB_5\rangle_1 \underset{k_b}{\overset{k_f}{\rightleftarrows}} \langle AB_5\rangle_0 + \langle AB_5H\rangle_1 \quad (7)_1$$

$$\langle AB_5H\rangle_1 + \langle AB_5\rangle_2 \underset{k_b}{\overset{k_f}{\rightleftarrows}} \langle AB_5\rangle_1 + \langle AB_5H\rangle_2 \quad (7)_2$$

$$\langle AB_5H\rangle_j + \langle AB_5\rangle_{j+1} \underset{k_b}{\overset{k_f}{\rightleftarrows}} \langle AB_5\rangle_j + \langle AB_5H\rangle_{j+1} \quad (7)_{j+1}$$

$$\langle AB_5H\rangle_{n-1} + \langle AB_5\rangle_n \underset{k_b}{\overset{k_f}{\rightleftarrows}} \langle AB_5\rangle_{n-1} + \langle AB_5H\rangle_n \quad (7)_n$$

where k_f and k_b are the kinetic constants of the equilibrium reactions.

This set of equations can be illustrated by all the curved arrows in the Fig. 7b, which represent the jumps of the H-atoms from a reduced site toward the adjacent oxidized site.

Assuming an isotropic diffusion in the material, k_f and k_b are thus equal (k_f=k_b=k), and it was already shown [21,24] that the constant k is linked to the diffusion coefficient used in the Fick's Law through the relationship:

$$D_H = kC_0\varepsilon^2 \quad (8)$$

where C_0 is the number of sites in which a H can be inserted (per cm^2), ε the thickness of a layer, and D_H the diffusion coefficient of H.

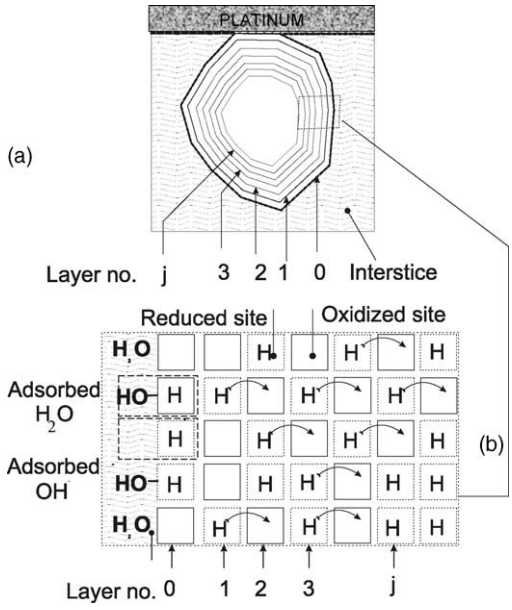

Fig. 7. Multilayer structure within a grain (a), and magnification of the multilayer structure near the surface of a grain (b). Arrows indicate some of the possible inserted-H jump between two adjacent layers.

4.3. Comments on peaks A_1 and A_2

The peak A_1 and the shoulder A_2 correspond to a mechanism that can be described by the reverse mechanism of the reduction reactions. This deconvolution suggests that deinsertion occurs in several steps with close kinetics. First, the electrochemical reaction occurs at the interface with the oxidation of H that was included in the material bulk (reverse of Eq. (4)). The H diffusion toward external sites is then the backward route of the equilibrium $(7)_i$. As $\langle AB_5H\rangle_0^{abs}$ is a surface reduced site, it can no longer lodge anymore the H-atoms coming from the internal sites. When, all the peripheral reduced sites are occupied by adsorbed species, an inert layer is produced. This prevents the electrochemical oxidation (4) occurring until desorption of a part of these species.

The width of peak A_1 at the lower scan rate ($0.01\,V\,s^{-1}$) is around 160 mV and becomes wider when the scan rate

increases. The theoretical value for peak width can be calculated by the relationship obtained for a closed electrochemical system that obeys the Butler–Volmer relationship (9):

$$W_{1/2}\ (\mathrm{mV}) = \frac{2RT}{\alpha nF} \tag{9}$$

where F, R, and T have their usual significance, n is the number of electron exchanged and α is the transfer coefficient ($\alpha = 0.5$). The experimental peak width when the scan rate is low, is much larger than the theoretical value if considering a simultaneous exchange of 5.5 electron per AB_5 unit (∼19 mV). As it is widely admitted, the electron-exchange reaction would involve only one electron: in that case, the theoretical peak width value is about 103 mV and is rather in good agreement with the experimental one. At low scan rates, the electrochemical signal gives no information on different occupancy sites for H, whereas different sites have been evidenced in chemical hydrogenating [25–27]. The relationship (9) also indicates that the peak width $W_{1/2}$ is independent of the scan rate. However, a broadening of the peak involving a decrease of n or α must be ruled out. Thus, such a broadening should be attributed to an electrode polarization due to the consumption of ionic species and water molecules. This is consistent with our previous remark and the estimation we have done for the consumption of the species inside the cavity of the electrode.

Elsewhere, a point to clarify is the shape difference between the charge and the discharge peaks.

4.4. Comments on plateau and peak C_4

The plateau that follows the smooth fall of the peak A_1 exhibits a small positive slope (Fig. 2). Most part of this current (corresponding to the horizontal part of the voltammogram for the more positive potentials) must be attributed to the capacitive current related to the grain periphery and the platinum collector interfaces. The residual current which is responsible for the positive slope of the plateau is due to the oxidation of the surface sites of the collector producing metal oxide PtO_x.

The peak C_4 is due to the reduction of the PtO_x formed during the anodic sweep. It is only observable when the scan rate v is sufficiently large because:

- First, the amount of these oxides is small. Assuming a monolayer hydrogen adsorption charge of 210 μC cm^{-2}, the exchanged charge is equal to about 5×10^{-9} C for the H oxidation for a Pt collector of 25 μm diameter. Supposing a two-electron transfer for the oxide formation, the charge is about 10^{-8} C.
- Second, the charge for the $LaNi_{3.55}Mn_{0.4}Al_{0.3}Co_{0.75}$ dramatically decreases for high scan rates (see Fig. 4c) while it is constant for the PtO_x.

4.5. Positive current cathodic peaks C_2 and C_3

Generally, this kind of peak can be observed during the cathodic scan when depassivation phenomena are implicated. Depassivation involves an inert film formed during the previous anodic scan, which prevents the oxidation reaction normally progressing. It corresponds to the destruction of this inert film during the cathodic scan. In the present case, the inert film and the depassivation process can be identified to the adsorbed H_2O produced during the oxidation (backward way of reaction 4). As a result, the reverse reaction of the electrochemical equilibrium (4) should rather be written as a two steps reaction:

$$\langle AB_5H\rangle_0^{ads} + OH^- \rightleftarrows \langle AB_5(H_2O)_{ads}\rangle_0 + e \tag{10}$$

that is followed by a chemical equilibrium describing the adsorption/desorption of water molecules from the interface electrode/electrolyte:

$$\langle AB_5(H_2O)_{ads}\rangle_0 \underset{k_b^{H_2O}}{\overset{k_f^{H_2O}}{\rightleftarrows}} \langle AB_5\rangle_0 + H_2O \tag{11}$$

The positive current is observed when the reaction $(7)_1$ is becoming predominant vis-a-vis of the reaction of desorption of the oxidized products within the potential range of the peak A_1. This involves that the reaction $(7)_1$ is blocked during the precedent anodic scan, i.e. both amount of H_2O adsorbed is large and its kinetic constant of desorption $k_f^{H_2O}$ is small. Therefore, the intensity of the peak C_2 is related to both ratio $v/k_f^{H_2O}$ and potential where the scan is reversed.

4.6. Long cycling evolution

We point out that the overall shape of voltammograms does not significantly change during the cycling. Thus, these curves illustrate a good performance of the material against the insertion and deinsertion of H-atom although the discharge depth reaches 100%, because the end of the peak fall is also the end of the discharge. A 50 mV s^{-1} scan rate corresponds to duration of around 12 s that is to say in drastic discharge conditions. The charge corresponds to the cathodic peak C_1. Taking into account the time for scanning whole this peak, the charge is also carried out in drastic conditions.

Some erratic variation was also observed with some sample electrodes. They must be attributed to internal rearrangement of the grains within the microcavity and to modifications of the texture of the material, which is caused by the H_2 evolution when the potential corresponds to the reduction of the solvent wall.

5. Conclusion

An hydride material, showing high technological interest, has been studied with the cavity microelectrode. This

shows the strong ability of this technique to work with different kinds of materials. Very high scan rates (a few $V\,s^{-1}$), as compared to those obtained with macroelectrodes (a few $mV\,s^{-1}$ in best cases) can be reached owing to the absence of significant polarisation effects. Within the range of $50\,mV\,s^{-1}$, the kinetic limit of the hydride material reached demonstrating the excellent kinetic response of those materials. Therefore, the limitations observed with conventional electrodes are to be attributed to the electrode environment rather than to the material itself. The great advantage of the cavity microelectrode technique is the possibility to perform electrochemical cycling at high scan rate in a short lapse of time. This allows evidencing the excellent ability of the material studied here to withstand thousands of cycles without important losses of capacity that could be attributed to corrosion effects. Such discrimination was never observed before, because effects of ageing in electrolyte are combined with cycling effects in conventional cycling studies. The possibility to use the cavity microelectrode to separate calendar corrosion and cycling corrosion will be further studied on different $LaNi_5$ substituted materials.

References

[1] J.O. Besenhard, in: Handbook of Battery Materials, Wiley, New York, 1999, pp. 209–230.
[2] F. Cuevas, J.-M. Joubert, M. Latroche, A. Percheron-Guégan, Appl. Phys. A 72 (2001) 225.
[3] J.J. Reilly, Z. Phys. Chem. N. F. 117 (1979) 155.
[4] A. Percheron-Guégan, J.C. Achard, J. Sarradin, G. Bronoël, in: Proceedings of the International Symposium on Hydrides for Energy Storage, Geilo, Norway, Pergamon Press, New York, 1978, p. 485.
[5] M.V. Simicic, M. Zdujic, D.M. Jelovac, P.M. Rakin, J. Power Sources 92 (2001) 250.
[6] K. Hong, J. Power Sources 96 (2001) 85.
[7] Z. Chen, Z. Chen, Y. Su, M. Lü, D. Zhou, P. Huang, Mater. Res. Bull. 33 (1998) 1449.
[8] C. Iwakura, T. Oura, H. Inoue, M. Matsuoka, Electrochim. Acta 41 (1996) 117.
[9] M. Ikoma, H. Kawano, I. Matsumoto, N. Yanagihara, Eur. Patent Appl. 271 (1987) 43.
[10] H. Ogawa, M. Ikoma, H. Kawano, I. Matsumoto, J. Power Sources 12 (1988) 393.
[11] V. Vivier, C. Cachet-Vivier, B.L. Wu, C.S. Cha, J.-Y. Nédélec, L.T. Yu, Electrochem. Solid-State Lett. 2 (1999) 385.
[12] V. Vivier, C. Cachet-Vivier, S. Mezaille, B.L. Wu, C.S. Cha, J.-Y. Nédélec, M. Fedoroff, D. Michel, L.T. Yu, J. Electrochem. Soc. 147 (2000) 4252.
[13] V. Vivier, C. Cachet-Vivier, C.S. Cha, J.-Y. Nédélec, L.T. Yu, Electrochem. Commun. 2 (2000) 180.
[14] A. Merzouki, C. Cachet-Vivier, V. Vivier, J.-Y. Nédélec, L.T. Yu, N. Haddaoui, J.-M. Joubert, A. Percheron-Guégan, J. Power Sources 109 (2002) 281.
[15] J.-M. Joubert, M. Latroche, R. Cerný, A. Percheron-Guégan, K. Yvon, J. Alloys Comp. 208 (2002) 330–332.
[16] K. Tammeveski, M. Arulepp, T. Tenno, C. Ferrater, J. Claret, Electrochim. Acta 42 (1997) 2961.
[17] A. Lundqvist, G. Lindbergh, Electrochim. Acta 44 (1999) 2523.
[18] Y. Leng, J. Zhang, S. Cheng, C. Cao, Z. Ye, Electrochim. Acta 43 (1998) 1945.
[19] J. Han, F. Feng, M. Geng, R. Buxbaum, D.O. Northwood, J. Power Sources 80 (1999) 39.
[20] V. Vivier, Ph.D. Thesis, University of Paris, 12 May 2000.
[21] E. Laviron, J. Electroanal. Chem. 112 (1980) 1.
[22] E. Laviron, L. Roullier, C. Degrand, J. Electroanal. Chem. 112 (1980) 11.
[23] E. Laviron, J. Electroanal. Chem. 122 (1981) 37.
[24] C.P. Andrieux, J.M. Saveant, J. Electroanal. Chem. 111 (1980) 377.
[25] A. Percheron-Guégan, C. Lartigue, J.C. Achard, P. Germi, F. Tasset, J. Less-Com. Met. 74 (1980) 1.
[26] M. Latroche, J. Rodriguez-Carvajal, A. Percheron-Guégan, F. Bourrée-Vigneron, J. Alloys Compd. 218 (1995) 64.
[27] A. Percheron-Guégan, C. Lartigue, Mater. Sci. Forum 31 (1988) 125.